

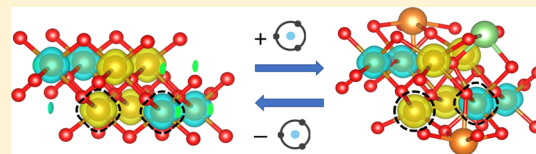
Intercalation-Driven Reversible Switching of 2D Magnetism

Arnab Kabiraj*¹ and Santanu Mahapatra

Nano-Scale Device Research Laboratory, Department of Electronic Systems Engineering, Indian Institute of Science (IISc) Bangalore, Bangalore 560012, India

S Supporting Information

ABSTRACT: The recent discovery of magnetism in atomically thin chromium triiodide has initiated the quest for two-dimensional magnetic materials. In an alternate route, here we explore the reversible switching of magnetism in naturally antiferromagnetic monolayer ferrous dioxide. Our high-throughput spin-polarized density functional theory calculations reveal antiferromagnetic to ferrimagnetic switching through the manipulation of the local magnetic moments mediated by lithium and magnesium ion intercalation. Hardware-accelerator-assisted rigorous ab initio computations involving structure searching, molecular dynamics, adaptive kinetic Monte Carlo, and hybrid functionals ensure sustainability of such switching amid randomness, structural deformation, thermal vibrations, and environmental conditions. The proposed technique along with conventional lithography may be used to create selective magnetic zones in a macroscopically nonmagnetic material for spintronics and memory devices.



INTRODUCTION

Recent advances in nanotechnology along with significant strides made in spintronics^{1,2} and valleytronics^{3,4} have intensified the search for magnetism in two-dimensional (2D) materials. The fact that these materials could also find essential applications in the field of sensing and memory technology⁵ has spurred the quest for 2D magnetism even more. Although once thought as impossible to exist in 2D materials,⁶ recent experiments find the presence of long-range ferromagnetic (FM) order at finite low temperatures in atomically thin CrI₃⁷ and Cr₂Ge₂Te₆.⁸ Further observation of long-range antiferromagnetic (AFM) order in FePS₃^{9,10} was indeed possible because of the strong magnetic anisotropy in these 2D materials. Very recently,¹¹ strong ferromagnetism in monolayer VSe₂ was discovered even at room temperature. Since then a host of 2D FM and AFM materials^{12–17} have been theoretically predicted and studied. However, these studies only address intrinsic 2D magnetism, whereas one extremely important aspect could be switchable or tunable magnetism controllable by external perturbations. AFM to FM transition in 2D materials has already been achieved with the application of an electric field¹⁸ and may also be attained with strain engineering.¹⁹ Charge or carrier doping has also been found to be an effective method of inducing ferromagnetism in nonmagnetic low-dimensional materials.^{20–23}

Apart from their applications in different domains of electronics, 2D materials have attracted much attention as possible electrode materials in next-generation cationic batteries due to their high surface-to-volume ratio.²⁴ Intercalation of cations in a 2D material changes its physical, chemical, and electronic properties significantly, which can be exploited for many other applications. Lithium (Li) intercalation has been used to induce semiconducting to metallic local phase transformation in MoS₂.²⁵ It has also found applications in organic electronics,²⁶ thermal circuits,²⁷ and

neuromorphic computing.²⁸ It is well known that Li intercalation can change the macroscopic magnetic moment of magnetic materials by modifying the oxidation states of the magnetic atoms locally.²⁹ Because of their large surface-to-volume ratios, in 2D materials, this effect should be very prominent since the intercalated Li can access almost all atoms from the surface to transfer its charge. The deintercalation then should theoretically return the material to its original magnetic state, ensuring reversibility in the change of magnetism. Such intercalation can be performed electrochemically (e.g., using the material as an electrode in a Li ion cell) or chemically (e.g., using a solution of a Li compound, most commonly butyllithium). In the recent past, at room temperature, intercalation-driven reversible tuning of magnetism has been demonstrated in nanopowdered α - and γ -Fe₂O₃ and MnFe₂O₄.^{30–32} It is worth noting that these ferrite materials already inherit macroscopic magnetism in their pristine form, and the Li intercalation only modulates its value. However, to achieve “magnetism switching”, the macroscopic magnetism of the pristine materials needs to be zero, which can subsequently be manipulated through intercalation.

We use high-throughput spin-polarized van der Waals density functional theory (DFT)-based calculations to predict the intercalation-driven reversible magnetism switching in naturally antiferromagnetic (AFM) iron dioxide (FeO₂), a recently predicted 2D material, discovered by computational exfoliation from its bulk counterpart.^{15,33} In a systematic approach, we first employ the “structure searching” technique to study the ferrimagnetism induction in pristine FeO₂ by different doses of pure Li, pure magnesium (Mg), and a mixture of Li and Mg intercalation. Among all, magnetism in a

Received: October 8, 2019

Revised: December 1, 2019

Published: December 5, 2019

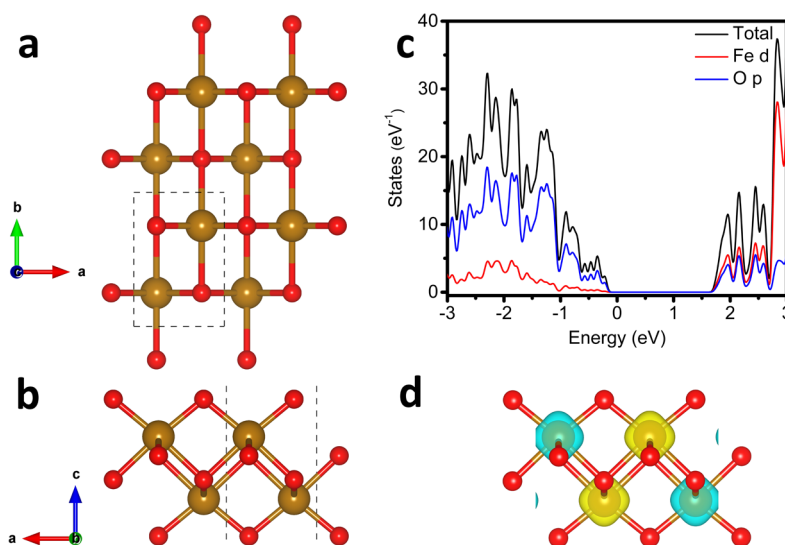


Figure 1. Pristine FeO₂ monolayer and its properties. (a) Top and (b) side view of a monolayer FeO₂ 2 × 2 supercell. Dashed lines indicate the boundary of the unit cell. Brown and red balls represent the Fe and O atoms, respectively. (c) Calculated DOS of the 2 × 2 FeO₂ supercell in the ground state AFM configuration (AFM4), which is the summation of the up- and down-spin components. These two components are not shown individually as they are identical in an AFM configuration. (d) Magnetization density isosurface for the FeO₂ supercell in the AFM4 configuration. Magnetization density is defined as $\rho_{\text{mag}} = \rho^{\uparrow} - \rho^{\downarrow}$, where ρ^{\uparrow} and ρ^{\downarrow} are up- and down-spin charge densities, respectively. Yellow clouds represent positive magnetization, and blue clouds represent negative magnetization. Isosurface level is set to 0.06 eV/Å³. All data in this figure have been obtained using HSE relaxations and calculations.

1:2 mixture of Li and Mg intercalated system is found to be more robust against the randomness, exhibits half-semiconducting nature, and thus is considered for further exploration. We then conduct ab initio molecular dynamics (AIMD) and adaptive kinetic Monte Carlo (AKMC) calculations to find that such induced magnetism is highly stable amid possible short- and long-time scale cation diffusion due to thermal energy. Strong magnetocrystalline anisotropy confirms the intercalated material to be a 2D Ising ferrimagnet with an in-plane magnetic moment. In spite of noticeable distortion introduced by the intercalated cations, the deintercalation algorithm finds the recovery of the original AFM state and affirms the reversibility of the magnetism switching. A two-level structure search technique is further employed to confirm the air stability of induced magnetism in the presence of oxygen (O₂) and water (H₂O) molecules. We also explore a hexagonal boron nitride (hBN) encapsulation method to protect the magnetism of the intercalated FeO₂. While similar studies in the literature rely entirely on semiempirical Hubbard *U* corrections, here we also use a rigorous hybrid functional for both structure relaxations and electronic structure calculations for most crucial results. Such massive computations with high rigor are achieved using hardware accelerators in place of conventional CPUs. The proposed technique may foster novel spintronic device design ideas since it can be used with conventional lithography²⁵ to create selective magnetic zones in a macroscopically non-magnetic material.

RESULTS

Material Properties. In their recent work, Mounet et al.¹⁵ used high-throughput computational exfoliation to predict 200+ “easily exfoliable” 2D materials based on known experimental bulk structures. Among these, naturally anti-ferromagnetic FeO₂, whose bulk parent is highly abundant in nature, appears to be dynamically stable from its phonon

spectrum.³³ The high optical phonon frequency (~20 THz) also suggests strong covalent bonding. Oxide materials are known for their excellent air stability. Also, 2D transition metal oxide (TMO) materials usually show exceptionally strong binding and a good amount of charge transfer with alkali metal ions.³⁴ On the basis of these virtues, we chose monolayer FeO₂ as the ideal material for our study.

For DFT calculations, the selection of a proper exchange-correlation functional for a specific system is of utmost importance, as local and semilocal DFT is known to incorrectly describe the strong on-site Coulomb interaction of localized d and f electrons, especially in iron oxides.³⁵ While the commonly used Perdew–Burke–Ernzenhof (PBE)³⁶ finds the material to be metallic,³³ the more rigorous and computationally challenging Heyd–Scuseria–Ernzerhof (HSE)³⁷ hybrid functional predicts it to be semiconducting. It is further observed that PBE with a semiempirical correction to the on-site Coulomb interaction added using a Hubbard *U* parameter (PBE+*U*) successfully describes the semiconducting nature of the material, albeit with an underestimated band gap. Since we implement high-throughput DFT calculations, which involve thousands of large crystal structures, the spin-polarized PBE+*U* formalism has been adopted to meet our computational budget. However, for the most crucial results, PBE+*U* solutions are benchmarked against the HSE formalism. In passing, we also note that the self-interaction-corrected local density approximation (SIC-LDA) functional along with the Korringa–Kohn–Rostoker coherent-potential-approximation (KKR-CPA) formalism is also being used to study dilute magnetic semiconductors.³⁸

Figure 1a and 1b illustrates the top and side view of the crystal structure of monolayer FeO₂. In a unit cell, only two magnetic configurations are possible, FM and AFM, where the AFM configuration has already been established as the ground state.³³ In this study, we mostly deal with a 2 × 2 supercell. We consider the most commonly occurring 5 AFM and the FM

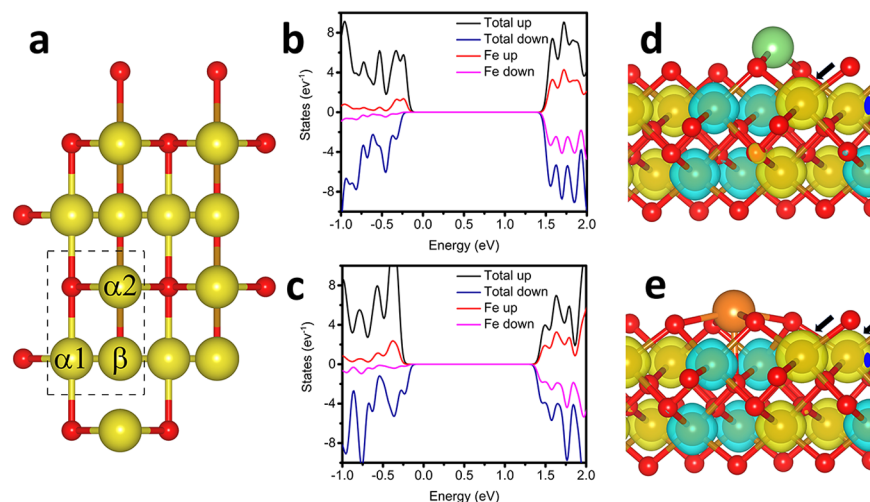


Figure 2. Single-cation adsorption. (a) Schematic of a fully intercalated 2×2 FeO_2 supercell. Yellow balls represent generic cations. Dashed line indicates the unit cell boundary. DOS of the FeO_2 supercell with (b) single Li adsorbed at $\alpha 1$ and (c) single Mg adsorbed at β , which are the most stable adsorption sites. Note that for all single-cation adsorption studies a large 4×2 FeO_2 supercell is used as the substrate to eliminate the unwanted cation–cation interaction from neighboring periodically repeated cells. Positive and negative DOS values represent the DOS of up- and down-spin electrons, respectively. Magnetization density of FeO_2 supercells with (d) single Li adsorbed at $\alpha 1$ and (e) single Mg adsorbed at β sites. Green and orange balls represent the Li and Mg atoms, respectively. Puffed magnetization clouds have been highlighted using black arrows. Iso-surface level is set to $0.06 \text{ eV}/\text{\AA}^3$. All data in this figure have been obtained using HSE relaxations and calculations.

configurations^{12,17} (see Supporting Figure 1) in a 2×2 supercell of the material to determine the ground state spin configuration. The “AFM4” (a kind of zigzag AFM) configuration is found to be the magnetic ground state by both PBE+ U and HSE calculations and is used for intercalation study. A comparison of lattice parameters, cohesive energies, and band-gap values calculated using different functionals is shown in Supporting Table 1. Figure 1c illustrates the HSE-calculated DOS of the AFM4 ground state. The HSE band gap of the material is found to be around 1.7 eV. From the DOS, it can be clearly seen that the valence band mostly consists of O-p orbitals and there is an almost equal contribution from Fe-d and O-p orbitals in the conduction band. Also, the DOS indicates strong hybridization between Fe-d and O-p orbitals, implying the existence of highly covalent bonds in the material. This is not surprising considering the reasonably high coordination number of atoms in the material and high frequencies of optical modes in the phonon spectrum.³³ A bond order analysis (see Supporting Raw Data) also supports this conclusion. Figure 1d depicts the magnetization density of the material. As expected, all of the positive as well as negative magnetization can be observed to be localized around the Fe atoms.

To test the thermal stability of the material, we perform an AIMD simulation at 300 K for more than 22 ps. The movement of the ions can be seen in Supporting Video 1, whereas Supporting Figure 2 depicts the fluctuation of total energy and temperature with time. The MD trajectory suggests excellent thermal stability of the material at room temperature.

In order to assess the strength of the AFM order in monolayer FeO_2 , we calculate the magnetocrystalline anisotropic energy (MAE) of the material including the spin–orbit coupling (SOC) effect and using both PBE+ U and HSE formalisms. The magnetic easy axis turns out to be in the in-plane $[010]$ direction, i.e., in the direction of the **b** vector, perhaps owing to the fact that the Fe–O bond lengths as well as Fe–O–Fe bond angles are much greater in this direction. While intrinsically FM 2D materials usually show an out-of-

plane easy axis, along the direction $[001]$,^{12,39,40} the occurrence of the in-plane easy axis in 2D AFM materials has been reported before.^{14,19} The MAE was found to be $E_{[010]} - E_{[001]} = -0.40 \text{ meV/Fe}$ and $E_{[100]} - E_{[001]} = 0.09 \text{ meV/Fe}$ using PBE+ U and $E_{[010]} - E_{[001]} = -1.04 \text{ meV/Fe}$ and $E_{[100]} - E_{[001]} = 0.15 \text{ meV/Fe}$ using HSE. The strong magnetic anisotropy of the material is comparable to most other FM and AFM monolayer materials^{12,14,19,41} and implies the presence of long-range Ising-like AFM order in 2D.

Magnetism Induction by Single-Cation Adsorption.

In this section, we study magnetism induction due to the adsorption of single Li and Mg cations in FeO_2 . Our primary aim is to inject as many electrons in the material as possible to induce the maximum amount of magnetism. Therefore, divalent Mg was considered along with monovalent Li. We also explored trivalent aluminum (Al); however, probably due to its p-shell valence electrons, the charge transfer to FeO_2 is found to be significantly less than that of Mg.⁴² Because the adsorption sites in FeO_2 for Li and Mg ions are not known beforehand, instead of intuitive approaches we use spin-polarized PBE+ U -based ab initio random structure searching (AIRSS)⁴³ to find them exhaustively. This random low-energy phase-finding algorithm usually is bias free (no local minima trapping) when compared to other similar algorithms^{44,45} and the implementation can be made highly parallelized⁴⁶ (see Methods). AIRSS has already been widely used for prediction of high-temperature and high-pressure phases^{47,48} of materials and is increasingly being used to study cation binding in monolayers.^{46,49,50}

Figure 2a shows all possible cation binding spots found by AIRSS in a 2×2 supercell of FeO_2 . Interestingly, because of the higher valency of Mg it can bind to 3 separate sites ($\alpha 1$, $\alpha 2$, and β) in the FeO_2 unit cell, whereas the Li ion can only be adsorbed in 2 such spots ($\alpha 1$ and $\alpha 2$). At both $\alpha 1$ and $\alpha 2$ sites the equilibrium cation adsorption spots are almost on top of the Fe atoms. However, only in the case of the $\alpha 2$ site, the nearest Fe atom to the cation is the Fe ion underneath it, as at $\alpha 1$ the cation is coordinated by 4 almost equidistance Fe

atoms. The exact coordination of the cations is listed in Table 1.

At the β site, the Mg ion gets adsorbed directly above an O atom. Similar to the $\alpha 1$ site, the Mg does not form a bond with the O atom directly beneath it but pulls 4 surrounding O atoms toward itself to form strong bonds. These bond formations and the charge transfers between the cations and the substrate can be clearly visualized using charge density difference isosurface plots (Supporting Figure 3). The amount of charge transferred from the cations to the substrate as computed by Bader charge analysis (see Table 1) affirms that the cations donate almost their entire outer s-shell electrons and exist in an ionized state after adsorption.

The single cation binding energy is calculated using the equation

$$E_b = E_{\text{FeO}_2+\text{cat}} - E_{\text{FeO}_2} - \mu_{\text{cat}} \quad (1)$$

where E_b is the binding energy of the single cation, $E_{\text{FeO}_2+\text{cat}}$ is the total energy of the single cation adsorbed in the FeO_2 structure, E_{FeO_2} is the energy of the pristine substrate, and μ_{cat} is the chemical potential of the bulk metallic phase of the cation adsorbed. According to this definition, a more negative binding energy would denote a stronger binding while positive binding energy would imply the possibility of formation of metal clusters and potential phase separation with the substrate. Irrespective of the functional used, the computed binding energies for all sites (see Table 1) are well below zero, indicating thermodynamically stable and exceptionally strong Li and Mg binding. In the case of Li, the most stable binding site is $\alpha 1$, whereas the most stable binding site for Mg is the β spot.

The DOS of the intercalated systems are depicted in Figure 2b and 2c and also in Supporting Figure 4. Clear disbalance between the up- and the down-spin components can be seen, where in the pristine material these two components are identical and therefore cancel each other out. Comparing with the DOS of the pristine substrate (Figure 1c) it appears that the extra injected electrons mostly make their way into the highly hybridized Fe-d–O-p orbitals, which are strongly localized around the Fe atoms and are responsible for the local magnetic moments in the material. In Table 1, the absolute magnetization of the supercells upon intercalation is listed. The DOS plots in Supporting Figure 4 illustrate why the Mg adsorbed at $\alpha 1$ and $\alpha 2$ does not result in any net magnetism but Li adsorbed at $\alpha 1$ and $\alpha 2$ and Mg at β does. Clearly, the net magnetism arises from the disbalance between the up- and the down-spin electrons caused by the extra injected electron(s) by the cation. While only the up-spin channel of the Fe-d–O-p orbitals in structures with Li adsorbed at $\alpha 1$ and $\alpha 2$ and Mg at β gets populated, both up- and down-spin channels get equally populated in the other cases. Complementing the DOS analysis, the visualization of the magnetism density (Figure 2d and 2e and Supporting Figure 5; also see Supporting Raw Data) also explains this observation. It can be observed that certain magnetization clouds near the adsorption sites have changed their shape and have increased in volume after adsorption. Bader magnetization analysis further reveals that the Fe atoms in these “puffed” magnetization clouds have an increased local magnetic moment $\mu \approx \pm 4.2 \mu_B$, where the normal Fe atoms show $\mu \approx \pm 3.5 \mu_B$, the same as the Fe atoms of the pristine substrate (see Supporting Raw Data). From here onward we shall call the

Table 1. Single Cation Adsorption in FeO_2

cation	site	$d_{\text{cation-Fe}}$ (Å)		$d_{\text{cation-O}}$ (Å)		E_b (eV)		Q_{transfer} (e)		Abs. mag (μ_B /supercell)	
		PBE+U	HSE	PBE+U	HSE	PBE+U	HSE	PBE+U	HSE	PBE+U	HSE
Li	$\alpha 1$	2.97, 2.98, 3.18, 3.21	2.97, 2.98, 3.18, 3.19	1.89, 1.94, 2.64, 2.91	1.88, 1.93, 2.67, 2.92	-3.97	-4.37	0.90	0.90	1	1
	$\alpha 2$	2.58, 3.72, 3.77, 5.08	2.56, 3.66, 3.74, 5.05	1.85, 1.86, 3.72, 3.72	1.84, 1.85, 3.72, 3.72	-3.91	-4.34	0.90	0.90	1	1
Mg	$\alpha 1$	2.84, 2.85, 2.88, 2.88	2.82, 2.83, 2.85, 2.86	1.94, 1.96, 2.04, 2.09	1.92, 1.94, 2.02, 2.07	-5.09	-5.62	1.66	1.68	0	0
	$\alpha 2$	2.65, 3.72, 3.78, 5.06	2.64, 3.66, 3.73, 5.02	1.85, 1.85, 3.70, 3.70	1.83, 1.83, 3.69, 3.69	-3.64	-4.04	1.64	1.69	0	0
	β	2.64, 2.64, 3.76, 3.77	2.62, 2.62, 3.72, 3.73	2.09, 2.09, 2.15, 2.15	2.07, 2.07, 2.13, 2.13	-5.24	-5.78	1.69	1.71	2	2

former the “high-spin” state and the latter the “low-spin” state. In Figure 2e two positive magnetization clouds can be seen becoming puffed where in Figure 2d only one such cloud has changed its shape and volume. Supporting Figure 5 shows that when Mg is adsorbed at $\alpha 1$ or $\alpha 2$, one positive and one negative magnetization cloud gets puffed while in other cases only the positive clouds change, yielding a net positive magnetism. It is worth noting that such mechanism of ferrimagnetic induction is different from conventional magnetic impurity-doped dilute magnetic semiconductors, where the ferromagnetic p–d exchange between the dopant and the host overcomes the antiferromagnetic double exchange to manifest FM behavior.⁵¹

Magnetism Induction by Multiple and Mixed-Cation Adsorptions. To increase the amount of induced magnetism, we study the effect of intercalation dosage. In a realistic scenario, selectively placing cations on specific sites in a material is not possible. It is always statistically likely that in an infinite crystal the disbalance created in one region will be countered by another region, resulting in zero net magnetism macroscopically as the local magnetization created this way can be completely random even in the phases with the same energy. As a possible remedy to this problem, we consider a few concentrations of mixed Li and Mg ion intercalation too. Again, we use AIRSS to find lowest energy intercalated phases for $\text{Li}_{0.25}\text{FeO}_2$, $\text{Li}_{0.375}\text{FeO}_2$, $\text{Li}_{0.5}\text{FeO}_2$, $\text{Mg}_{0.25}\text{FeO}_2$, $\text{Mg}_{0.375}\text{FeO}_2$, $\text{Mg}_{0.5}\text{FeO}_2$, $\text{Li}_{0.125}\text{Mg}_{0.25}\text{FeO}_2$, $\text{Li}_{0.125}\text{Mg}_{0.375}\text{FeO}_2$, and $\text{Li}_{0.375}\text{Mg}_{0.125}\text{FeO}_2$. The total energy of an intercalated structure for a particular concentration mostly depends on three factors: (i) adsorption at more stable binding sites produces more stable structures, (ii) cation–cation repulsion, which increases with increasing concentration of adsorbed cations, produces less stable intercalated phases, and (iii) deformation introduced in the substrate by adsorbed cations can produce more stable structures in terms of binding energy.⁴⁶ By bringing randomness into the fold, AIRSS takes care of all of these factors in an experiment-like manner to find the most stable phases. Although being computationally very expensive, AIRSS have reproduced real-life phenomena like electroplating⁴⁹ and bond cleavage in the substrate⁴⁶ well, which usually cannot be captured by manually made “uniform-adsorption” structures.

A 2×2 supercell of FeO_2 that provides a good balance between computational cost and degrees of freedom is used as the substrate for these structure searches. The most stable intercalated crystal structures found by AIRSS are shown in Figure 3. As anticipated, with increasing cation concentration the deformation in the substrate increases and the intercalated phases ultimately either turn into amorphous structures ($\text{Li}_{0.125}\text{Mg}_{0.375}\text{FeO}_2$) or change to commensurate new phases ($\text{Li}_{0.5}\text{FeO}_2$, $\text{Mg}_{0.5}\text{FeO}_2$, $\text{Li}_{0.375}\text{Mg}_{0.125}\text{FeO}_2$) with ample Fe–O broken bonds. Frequently, these severely deformed phases do not return to the pristine substrate structure upon deintercalation,⁴⁶ destroying the reversibility of the process. However, average binding energy in all of these AIRSS-found phases is well below zero, indicating stable cation binding. While focusing on the magnetism of these phases, we consider the top 5 lowest energy phases from every structure search to assess the consistency of the achieved magnetism upon intercalation. Figure 4 summarizes all of these magnetism data. Among the 9 concentration doses tried, 3 phases, namely, $\text{Li}_{0.5}\text{FeO}_2$, $\text{Mg}_{0.375}\text{FeO}_2$, and $\text{Mg}_{0.5}\text{FeO}_2$, show consistently zero magnetism in all of the top 5 structures, while others except

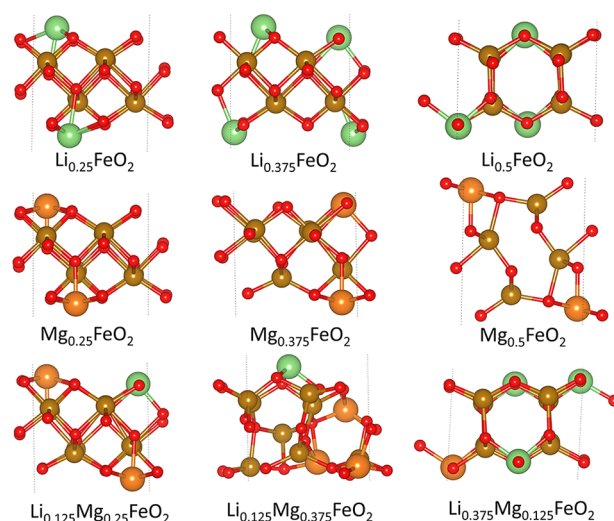


Figure 3. Most stable intercalated structures. Most energetically stable intercalated FeO_2 structures for various Li and Mg doses as found by AIRSS are shown. Note that a 2×2 FeO_2 supercell is used as the substrate in these structures. Dotted lines indicate the supercell boundary. All of these structures have been obtained using PBE+ U relaxations.

one phase ($\text{Li}_{0.125}\text{Mg}_{0.25}\text{FeO}_2$) yield random values in the range from -1 to $5 \mu_B$ in the 2×2 supercell. It is interesting to note that in a perfectly nondeformed structure one would expect the $\text{Li}_{0.375}\text{FeO}_2$ to show a maximum magnetization of $3 \mu_B$ because of the 3 electrons injected into the supercell. However, the top structure, which becomes moderately deformed upon adsorption, shows a magnetic moment of $5 \mu_B$ in its most energetically stable structure, highlighting the importance of structural deformation and the need for AIRSS. Most fascinatingly, the phase $\text{Li}_{0.125}\text{Mg}_{0.25}\text{FeO}_2$ shows a consistent magnetism of $3 \mu_B$ in all of its top 5 lowest energy structures, hinting at the possibility of robust magnetism amid randomness in this specific concentration.

To ensure the strength of the induced ferrimagnetic (FeM) order, we again calculate the MAE for all five $\text{Li}_{0.125}\text{Mg}_{0.25}\text{FeO}_2$ phases including SOC and using the PBE+ U formalism. The easy axis in all of the top five $\text{Li}_{0.125}\text{Mg}_{0.25}\text{FeO}_2$ phases turns out to be along the in-plane $[010]$ direction, i.e., the intercalation process does not alter the easy magnetization axis of the material. The MAE is found to be $E_{[010]} - E_{[001]} < -0.074$ meV/Fe and $E_{[100]} - E_{[001]} > 0.019$ meV/Fe (see Supporting Table 2) in all of the top 5 structures. HSE calculation on the top structure yields a much stronger MAE, $E_{[010]} - E_{[001]} = -0.218$ meV/Fe and $E_{[100]} - E_{[001]} = 0.022$ meV/Fe. Although the intercalation process weakens the magnetic anisotropy by almost five times, it still remains reasonably high and comparable to that of most other reported 2D FM and AFM materials.^{12,14,19,41} It should be noted that the MAE mentioned above is a somewhat average value in a supercell because all Fe ions do not contribute equally in the MAE in this FeM-intercalated material. However, the strong anisotropy of the material hints toward it being a robust Ising ferrimagnet with long-range order.⁴¹

Figure 5a shows the HSE DOS of the energetically top $\text{Li}_{0.125}\text{Mg}_{0.25}\text{FeO}_2$ structure. Even after injecting 5 electrons in the substrate supercell, the band gap of the material remains greater than 1 eV, achieving semiconducting ferrimagnetism. A significant amount of disbalance between the up- and the

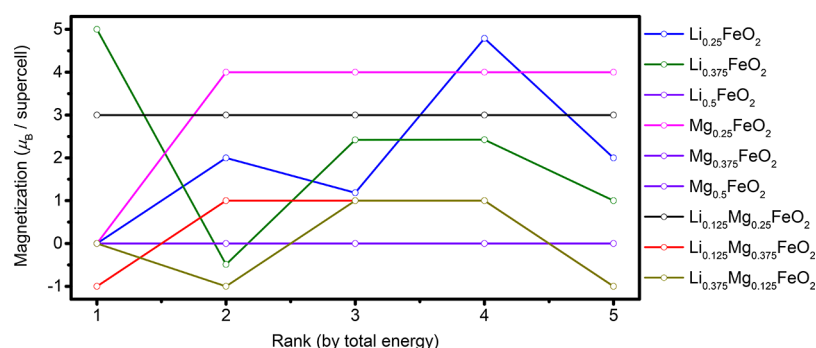


Figure 4. Magnetization variation with intercalation. Variation of the magnetic moment of the top 5 most stable structures with various doses of Li and Mg intercalation is shown. All of these data have been obtained using PBE+*U* static runs.

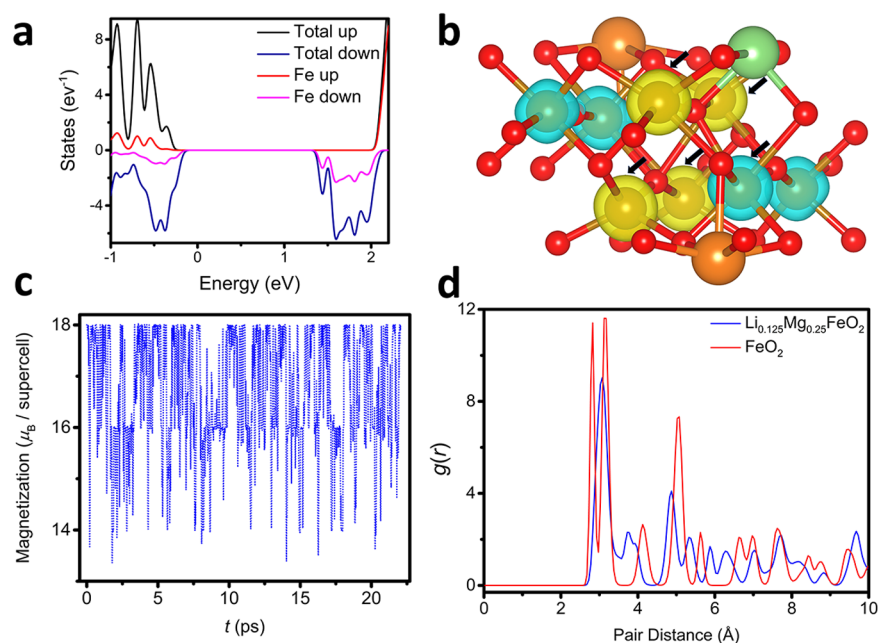


Figure 5. Properties of $\text{Li}_{0.125}\text{Mg}_{0.25}\text{FeO}_2$ phase. (a) DOS and (b) magnetization density of the energetically most stable $\text{Li}_{0.125}\text{Mg}_{0.25}\text{FeO}_2$ phase. Again, the puffed magnetization clouds have been highlighted using black arrows. (c) Variation of the magnetic moment of the $\text{Li}_{0.125}\text{Mg}_{0.25}\text{FeO}_2$ supercell with time during the MD run. (d) RDF of the Fe–Fe atom pair for the most stable $\text{Li}_{0.125}\text{Mg}_{0.25}\text{FeO}_2$ phase and for the pristine FeO_2 from their entire MD runs. Data depicted in a and b have been obtained using HSE relaxations and calculations, while other data have been obtained from PBE+*U* calculations.

down-spin components can be seen near the Fermi level. Also, both valence and conduction bands seem to be entirely contributed by down-spin electrons, suggesting the existence of a “half-semiconductor”. Figure 5b illustrates the HSE magnetization density isosurface (also see Supporting Figure 6) of this structure. Four puffed positive clouds and one puffed negative magnetism cloud localized around the Fe atoms are clearly visible, explaining the net magnetism of the supercell being $3 \mu_{\text{B}}$. Bader magnetism analysis confirms this too (see Supporting Raw Data). The top $\text{Li}_{0.125}\text{Mg}_{0.25}\text{FeO}_2$ structure is used for further stability analyses.

Reversibility and Stability of Induced Magnetism. In order to assess the reversibility of the intercalation process, we apply a simple but rigorous deintercalation algorithm⁴⁴ (see Methods) using the PBE+*U* formalism to the energetically most stable $\text{Li}_{0.125}\text{Mg}_{0.25}\text{FeO}_2$ structure. Supporting Video 2 shows a slideshow of the deintercalation processes. All deintercalated structures are found to be almost identical to the pristine monolayer FeO_2 structure, both visually and

energetically. Also, the net magnetism of these deintercalated phases is found to be zero, ensuring the complete reversibility of the magnetism induction process by intercalation.

In order to explore the short-term mechanical and magnetic stability with thermal vibrations, we again perform AIMD of the top $\text{Li}_{0.125}\text{Mg}_{0.25}\text{FeO}_2$ phase for more than 22 ps at 300 K. Figure 5c depicts the varying magnetism of the supercell with time (see Supporting Figure 7 for total energy and temperature variation). Although in some instances the magnetism can be seen reducing up to 25%, the large average magnetism confirms its robustness. The radial distribution function (RDF) between Fe–Fe atom pairs of the intercalated material along with the Fe–Fe RDF of the pristine FeO_2 is shown in Figure 5d. The same comparison between the RDFs of these two materials for pairs Fe–O and O–O can be found in Supporting Figure 7. The reduction of crystallinity is evident in these diagrams as the pair distance peaks broaden in the intercalated material significantly when compared with the pristine material. The whole MD trajectory can be found in

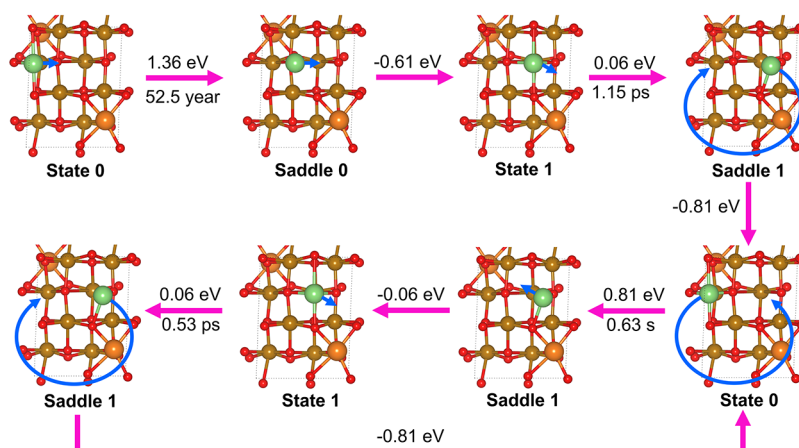


Figure 6. AKMC simulation. States and transitions observed during the AKMC simulation are summarized here. In each state or saddle point, the blue arrow indicates the next location of the Li ion. Saddle point heights and estimated time to overcome are written above and below the pink arrows. These have been estimated using PBE+*U* calculations.

Supporting Video 3. This along with the RDFs prove that the intercalated material preserves its induced magnetism at room temperature, albeit with less crystallinity.

In long time scale, adsorbed cations can diffuse on the surface of the monolayer, shifting to other stable adsorption sites. This could change the cation configuration ultimately changing the magnetism. To test the long-term behavior of the top $\text{Li}_{0.125}\text{Mg}_{0.25}\text{FeO}_2$ phase with possible cation movements we perform AKMC^{52,53} simulation. Figure 6 illustrates the events that occurred in the simulation, and Supporting Raw Data tabulates all of the states, their total energy, the diffusion barriers found, and the estimated time to make the transitions. To summarize, only one Li ion transition (State 0 \leftrightarrow Saddle 1 \leftrightarrow State 1) is found likely to occur in our time scale of interest (picoseconds to days). In both State 0 and State 1 (which is energetically slightly less stable) the magnetism remains the same because the overall disbalance between the injected electrons does not change.

To examine the air stability of the intercalated material we run a second level AIRSS on the already AIRSS-generated intercalated structure. In two different structure searches one O_2 molecule and one H_2O molecule was placed randomly in the supercell. Although this corresponds to a much greater concentration of these molecules than that of air at natural temperature and pressure, it provides a good idea about the possibility of any reaction. Figure 7a and 7b illustrated the AIRSS-found and HSE-optimized most energetically stable structures of $\text{Li}_{0.125}\text{Mg}_{0.25}\text{FeO}_2 + \text{O}_2$ and $\text{Li}_{0.125}\text{Mg}_{0.25}\text{FeO}_2 + \text{H}_2\text{O}$. Visually, it seems that the O_2 does not react with the material, but the H atoms of the H_2O form some hydrogen bonds with the O atoms of the material. However, in both cases, a bond order and charge partitioning analysis (see Supporting Raw Data) reveals a slight increase of bond order and slight loss of charge in the Mg atoms closest to the O atoms of the molecules, suggesting these indeed form a weak bond. Still, we find the magnetism of the intercalated material remains intact, proving the robustness of the induced magnetism in air. Because the O_2 molecule itself is paramagnetic, we again perform an MAE calculation on the O_2 -adsorbed top structure using PBE+*U*. The MAE was found to be $E_{[010]} - E_{[001]} = -0.094$ meV/Fe and $E_{[100]} - E_{[001]} = 0.022$ meV/Fe, slightly stronger than the MAE of the $\text{Li}_{0.125}\text{Mg}_{0.25}\text{FeO}_2$ top structure. However, this is probably

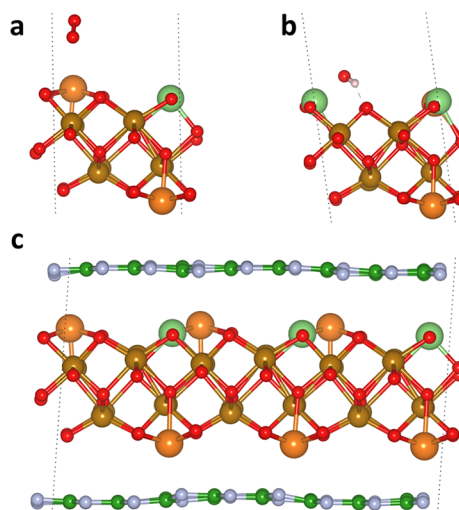


Figure 7. Environment effect. Most energetically stable (a) $\text{Li}_{0.125}\text{Mg}_{0.25}\text{FeO}_2 + \text{O}_2$, (b) $\text{Li}_{0.125}\text{Mg}_{0.25}\text{FeO}_2 + \text{H}_2\text{O}$ phases, and (c) monolayer hBN encapsulated $\text{Li}_{0.125}\text{Mg}_{0.25}\text{FeO}_2$ phase. Pink, blue, and green balls represent H, N, and B atoms, respectively. These structures have been obtained using HSE relaxations.

because we could not factor in the localization of the p orbitals in the O_2 molecule, which gives rise to its paramagnetism. Qualitatively, we can say that the MAE of the intercalated material is not disturbed by the paramagnetic O_2 adsorption.

Since the value of the induced magnetism in the intercalated structure is not large, we also explored an all-2D encapsulation strategy to protect it from other environmental effects. Hexagonal boron nitride (hBN) monolayers are large band gap dielectric materials known to be inert and have been used as an encapsulating material.⁵⁴ Here, we try to encapsulate the intercalated FeM structure, placing monolayer hBN sheets both on the top and on the bottom of the material. The sheets were rotated to make a supercell containing 177 atoms to achieve an initial strain (before relaxation) below 1.5%. Figure 7c shows the HSE-relaxed hBN-encapsulated structure. The N atoms in the hBN sheets have buckled slightly close to the adsorbed Mg atoms, hinting at a bonding interaction between the two. Again, a slight increase in the bond order and slight loss of charge in the Mg atoms (see Supporting Raw Data)

have been discovered using bond order and charge partitioning analysis, confirming the existence of weak Mg–N bonds. However, the amount of magnetism is found to be being intact in the encapsulated structure. The structure's mechanical (see Supporting Video 4) and magnetic stability (see Supporting Figure 8) at room temperature is also verified with AIMD calculations. Therefore, the encapsulation strategy using hBN monolayers could prove to be effective in protecting the intercalation-driven magnetism.

Effect of Spin Fluctuations. In order to determine the pristine monolayer material's Néel temperature (T_N), we use the total energies of different AFM and FM configurations to fit the parameters of an effective Heisenberg model Hamiltonian^{19,55}

$$H = -\frac{1}{2} \sum_{ij} J_1 \mathbf{S}_i \cdot \mathbf{S}_j - \frac{1}{2} \sum_{i,k} J_2 \mathbf{S}_i \cdot \mathbf{S}_k - A \sum_i (S_i^y)^2 \quad (2)$$

where J_1 and J_2 are the nearest-neighbor (NN) and the next-nearest neighbor (NNN) exchange coupling constants, \mathbf{S}_i and \mathbf{S}_j are the spins at site i and j , respectively, and A is the magnetic anisotropy constant. S is computed as $\mu/(2\mu_B)$, where μ is the local magnetic moment of the Fe ions. Conducting the Bader charge and magnetization analysis (see Supporting Raw Data), we find $\mu = \pm 3.47 \mu_B$ using HSE. This results in a converged value of NN coupling, $J_1 = -28.89$ meV, and NNN coupling, $J_2 = -2.7$ meV, for HSE (see Supporting Methods and Supporting Raw Data for details). For 2D materials, a classical Monte Carlo-based solution of the Heisenberg model is known to accurately predict the transition temperature,⁵⁵ and using the same we obtained the AFM to PM transition temperature of monolayer FeO₂ as 63 K (see Supporting Figure 11).

Direct study of the FeM to PM transition at finite temperatures becomes extremely challenging for the intercalated Li_{0.125}Mg_{0.25}FeO₂ material because of significant lattice distortion and asymmetry introduced by the adsorption process, which blurs the distinction between nearest neighbors and next nearest neighbors. Even if a symmetric lattice is assumed, the number of different exchange coupling constants increases manyfold, which again makes it virtually impossible to solve for them. However, a recent study demonstrates about a 33% increase in Curie temperature in monolayer FM Cr₂Ge₂Te₆ upon lithiation.⁵⁶ From the RDF plotted in Figure 5d it can be clearly observed that the closely situated Fe–Fe NN and NNN peaks merge together at room temperature after the intercalation, which implies that the NNNs also become NNs in the intercalated material due to slight changes in Fe–Fe bond lengths. This suggests that the magnetic NN coordination number in the material can increase up to 3 times after intercalation, which could push the Curie temperature of the material much further. The MD and AKMC studies, where the effect of spin fluctuations are not captured, have been performed at room temperature as an upper limit.

DISCUSSION

Although here we show intercalation-driven AFM to FeM transition, in principle, nonmagnetic materials might also be turned into AFM or FM materials by electron injection. In the latter case, a much larger magnetic moment is expected since the magnetism does not depend on the statistical disbalance between the number of up and down spins. It is worth noting

that the monolayer FeO₂ inherits a crystal structure similar to that of intrinsically FM monolayers of chromium oxyhalides.¹² However, the lattice parameter b is almost 1.5 times larger than a in the former case, while both are almost the same in the case of CrOCl and CrOBr.³³ While a detailed analysis is out of the scope, our initial PBE+ U calculations suggest an AFM to FM transition in FeO₂ with an application of 10% uniaxial compressive strain along b , possibly because the compressed Fe–O bond angles ultimately satisfy the Goodenough and Kanamori criterion.^{57,58} We also note that a hexagonal phase of monolayer FeO₂⁵⁹ exhibits an FM ground state. Again, the bond angles of this particular phase explain this apparent discrepancy. Unlike its rectangular counterpart, the Fe–O–Fe bond angles are very close to 90° in this hexagonal FeO₂, which promotes FM superexchange.

In general, to achieve such intercalation-driven switchable magnetism the substrate material must be capable of adsorbing two kinds of cations with different valency. The charge transfer from the cation to the substrate needs to be high. The material must be mechanically strong to bear repeated intercalation–deintercalation cycles. Monolayer FeO₂ satisfies all of these requirements with its bulk parent being abundant in nature. From our study it also appears that FeO₂ might be an attractive electrode material for lithium and magnesium ion batteries.

In summary, here we use high-throughput first-principles-based calculations to demonstrate the fact that the intercalation of mixed cations of different valency can be used to induce robust magnetism in a naturally antiferromagnetic two-dimensional material. The process, which can be implemented electrochemically or chemically, is compatible with conventional lithography and might be used to create selective magnetic zones in a macroscopically nonmagnetic material. Very dense FeM–AFM alternating structure in a single crystal can also be produced, which could find applications in spintronics and memory technology. The reversibility of induced magnetism may be useful in realizing nonvolatile programmable logic devices.

METHODS

DFT Calculations. Spin-polarized DFT calculations are carried out using the generalized gradient approximation (GGA) as implemented in the code VASP^{60–63} with the PAW⁶⁴ method using the Perdew–Burke–Ernzerhof (PBE)³⁶ exchange correlation and the Heyd–Scuseria–Ernzerhof (HSE)³⁷ hybrid functionals. Specifically, the HSE06 variant is used here which is known to predict accurate properties for most systems.⁶⁵ For most calculations, a correction on strongly correlated Fe 3d electrons (PBE+ U) is applied using the Dudarev⁶⁶ formulation. A semiempirical van der Waals (vdW) dispersion correction is applied via the Tkatchenko–Scheffler method (TS)⁶⁷ with iterative Hirshfeld partitioning⁶⁸ for both PBE+ U and HSE calculations. A slightly larger $s_R = 0.96$ is used for HSE calculations with this scheme.⁶⁹ The following electrons have been treated as valence electrons and are expanded in the plane-wave basis set: Fe, 3d⁷4s¹; O, 2s²2p⁴; Li 2s¹2p⁰; Mg, 3s²3p⁰. For all calculations, a sufficiently large cutoff energy of 550 eV is used to avoid any Pulay stress. For all structural relaxations, except one, a $\frac{30}{a} \times \frac{30}{b} \times \frac{30}{c}$ Monkhorst–Pack k -points grid is used to sample the Brillouin zone, where a , b , and c are the lengths of the lattice parameters of the particular supercell. Only the HSE relaxation for the hBN-encapsulated structure containing 177 atoms is per-

formed using the gamma-point-only sampling. A denser $\frac{40}{a} \times \frac{40}{b} \times 1$ gamma-centered k -points mesh is applied for HSE static calculations, and a $\frac{60}{a} \times \frac{60}{b} \times \frac{60}{c}$ similar k -mesh is used for all other static runs. Electronic convergence is set to be attained when the difference in energy of successive electronic steps becomes less than 10^{-6} eV, whereas the structural geometry is optimized until the maximum Hellmann–Feynman force on every atom falls below 0.01 eV/Å. For the high-precision MAE calculations, a stricter electronic convergence criterion of 10^{-8} eV for PBE+ U and 10^{-7} eV for HSE is imposed. A large vacuum space of ≥ 28 Å in the direction of c is applied to avoid any spurious interaction between periodically repeated layers. The Bader charge and magnetization analysis is performed using the code developed by the Henkelman group,^{70–73} where charge densities generated from DFT static runs are used as inputs. All crystal structures and isosurfaces are generated using the tool VESTA.⁷⁴ More details can be found in [Supporting Methods](#).

Determination and Limitation of U . The value of the effective U is determined from the 2×2 supercell using the linear-response approach.⁷⁵ It is found that using a 3×3 supercell changes the value of U negligibly but imposes severe computational load. The different FM and AFM configurations are tested using this value of U . After finding the ground state spin configuration, the U is determined again for this configuration, and the structure is relaxed. This cycle is repeated to obtain a converged value of $U = 4.38$ eV. This value is used throughout this work. Also, the spin configurations are again tested with this value to make sure the ground state does not change with changes in U .

Clearly, the above-mentioned process for determining U is extremely tedious but necessary as experimental data is not available for monolayer FeO₂ to benchmark the PBE+ U results. Ideally, if there is a change in the crystal structure or change in the number of d electrons, the U should be recalculated. Our studied intercalation process induces both deformation in the lattice and a change of oxidation states in few atoms near the adsorption sites. However, because we examine thousands of large supercells in a high-throughput manner, determining U for each and every structure is practically impossible. Therefore, we use the value of U determined for the pristine FeO₂ also for the intercalated systems. Whenever possible we use the more rigorous but computationally demanding HSE formalism to benchmark the crucial results since it does not require any semiempirical parameters like U , even for strongly correlated systems. [Table 1](#) shows that apart from the binding energy, PBE+ U -calculated values are in excellent agreement with those of HSE.

For an ultimate benchmarking exercise, we relax and perform a static run on the lowest energy Li_{0.125}Mg_{0.375}FeO₂ phase using both PBE+ U ($U = 4.38$ eV) and HSE. The reason for choosing this phase is that it has the most electrons among our tested intercalated structures and is the most deformed structure. For this structure the average binding energy is -5.04 eV/cation using PBE+ U and -5.68 eV/cation using HSE. For an almost amorphous and high amount of electron-injected structure, these values seem remarkably close, justifying our decision to use a constant U throughout. Note that the magnetism of the supercell, which is our main property of interest, is always predicted to be the same using PBE+ U and HSE.

AIRSS Calculations. Adsorbates are placed on the top and bottom of the substrate supercell randomly using the AIRSS initial configuration generation engine and are subsequently relaxed to their nearest local minima using DFT. The (x, y) fractional coordinates of the adsorbate molecules or ions are allowed to be completely random, but depending on the atomic radii, the minimum separation between pairs of atoms is kept between 0.9 and 1.8 Å to minimize atomic overlaps. The vertical distance (along c) of the adsorbates from the surface is chosen randomly from the range of 1.2–4.8 Å (see [Supporting Figure 9](#)). For each search, ≥ 150 random structures that could be relaxed successfully are explored. The AIRSS lowest energy phase-finding algorithm and its highly parallel master–slave implementation are similar to that of our previous work.⁴⁶ A lighter $2 \times 1 \times 1$ k -mesh with PBE+ U formalism is used to relax the structures while searching for the lowest energy phases. However, the top five lowest energy structures from every energy-rank list are processed further with the above-mentioned stringent DFT setup.

AIMD and AKMC Simulations. For both pure FeO₂ and Li_{0.125}Mg_{0.25}FeO₂ top structure, a 6×4 supercell for the substrate is chosen for AIMD runs, resulting in supercells with 144 and 162 atoms, respectively. The PBE+ U formulation is used for the AIMD runs with gamma-point-only sampling. A canonical ensemble (NVT) is used, and a Nosé–Hoover thermostat^{76,77} at 300 K is employed. The simulations are run for > 22 ps with a 5 fs time step.

The AIRSS-found top Li_{0.125}Mg_{0.25}FeO₂ structure is subjected to the AKMC simulation. The EON code^{52,53} developed by the Henkelman group interfaced with VASP is used for this. The simulation runs at 300 K, and based on the AIMD trajectory, all atoms except the adsorbates are assumed to be fixed in the long time scale. All adsorbates are displaced randomly at the same time to find the saddle points. The searches are continued until the confidence builds up to 0.95 in the current state. After that the system moves on to the next state depending on the calculated barrier heights and prefactors. The barriers higher than 2 eV are discarded as these are too large to consider for a state transition at 300 K. During the first transition of the simulation it can be seen that the estimated time to transition through a 1.36 eV barrier is 52.5 years, which justifies the above assumption further. For all saddle point searches and prefactor calculations with DFT, a $\frac{30}{a} \times \frac{30}{b} \times \frac{30}{c}$ k -points sampling and the PBE+ U formalism is used. Because almost 100 saddle searches are conducted during the whole simulation, it can be concluded that the Mg ions always face a barrier > 2 eV in the top Li_{0.125}Mg_{0.25}FeO₂ phase and therefore is unlikely to diffuse in the long time scale of years.

For all DFT calculations related to AIRSS, AIMD, and AKMC, instead of the TS dispersion correction, computationally lighter DFT-D3 dispersion correction as developed by Grimme⁷⁸ is employed.

Deintercalation Algorithm. Following the method proposed in [ref 44](#), a randomly chosen single cation is removed and the structure is allowed to fully relax with stringent DFT conditions using the PBE+ U formalism. We only explore three deintercalation paths since these sequential calculations are computationally expensive. [Supporting Video 2](#) shows a slideshow of the deintercalation process. The starting, intermediate, and final magnetism during this process are plotted in [Supporting Figure 10](#).

Hardware Accelerator-Based Parallel Computation.

Hardware accelerators, namely, NVIDIA Tesla K40 GPUs and Intel Xeon Phi KNL manycore processors (see [Supporting Methods](#)), are used extensively in our work, which is found to provide a significant speedup over conventional CPUs. For instance, the 144-atom supercell relaxation using spin-polarized vdW-corrected PBE+*U* has taken only ~16 h using 24 such GPUs. However, for HSE relaxations, the VASP 5.4.4 GPU port is found to be unsuitable in our case, yielding erroneous energies and forces, even with ALGO = All, Damped, and Normal. As a result, the PBE+*U* relaxed 144-atom structure is further HSE relaxed using 748 KNL cores, which takes around 72 h. This is still quite fast considering the huge computational load of the spin-polarized vdW-corrected HSE calculation for a 144-atom supercell. Because of restrictions in the supercomputer used, we could only use one MPI rank per GPU, which is definitely suboptimal. However, we try to make up for it by tuning the NSIM parameter and using *k*-points parallelization as much as possible. For our calculations, NSIM = 24 is found to be optimal, which along with *k*-points parallelization provided a significant speed boost in GPUs. The *k*-points parallelization along with band parallelization is also used extensively in KNL-based computations to take full advantage of its many-core architecture. While real space projection has been used for all relaxations, only reciprocal space projection is employed in static runs to get accurate energy and magnetism values.

■ ASSOCIATED CONTENT

Supporting Information

The Supporting Information is available free of charge at <https://pubs.acs.org/doi/10.1021/acs.jpcc.9b09477>.

Figures for spin configurations, AIMD simulations, isosurface plots, density of states, AIRSS configuration, deintercalation magnetism evolution, and spin fluctuations; tables for DFT functional comparison and MAE; supporting computational methods ([PDF](#))

AIMD of FeO₂ ([MPG](#))

Deintercalation of Li_{0.125}Mg_{0.25}FeO₂ ([MPG](#))

AIMD of Li_{0.125}Mg_{0.25}FeO₂ ([MPG](#))

AIMD of hBN encapsulated Li_{0.125}Mg_{0.25}FeO₂ ([MPG](#))

■ AUTHOR INFORMATION

Corresponding Author

*E-mail: kabiraj@iisc.ac.in.

ORCID

Arnab Kabiraj: [0000-0002-7063-0169](https://orcid.org/0000-0002-7063-0169)

Author Contributions

A.K. performed the DFT calculations, implemented hybrid processor-based structure search, AKMC, deintercalation algorithm, and classical MC simulations, and analyzed the results. S.M. conceived the problem statement and overall supervised the work. All authors contributed to the writing.

Notes

The authors declare no competing financial interest.

Additional supporting raw data can be accessed from <https://osf.io/xnhr6/>.

■ ACKNOWLEDGMENTS

This work was partially supported by Space Technology Cell, Indian Space Research Organisation (ISRO), under Grant

ISTC/EED/SM/392. The authors thank the Supercomputer Education and Research Centre (SERC), Indian Institute of Science (IISc) Bangalore, for GPU- and Xeon-Phi-based computations.

■ REFERENCES

- (1) Han, W. Perspectives for Spintronics in 2D Materials. *APL Mater.* **2016**, *4* (3), 032401.
- (2) Feng, Y. P.; Shen, L.; Yang, M.; Wang, A.; Zeng, M.; Wu, Q.; Chintalapati, S.; Chang, C.-R. Prospects of Spintronics Based on 2D Materials. *Wiley Interdiscip. Rev. Comput. Mol. Sci.* **2017**, *7* (5), No. e1313.
- (3) Schaibley, J. R.; Yu, H.; Clark, G.; Rivera, P.; Ross, J. S.; Seyler, K. L.; Yao, W.; Xu, X. Valleytronics in 2D Materials. *Nat. Rev. Mater.* **2016**, *1*, 16055.
- (4) Farooq, M. U.; Hong, J. Switchable Valley Splitting by External Electric Field Effect in Graphene/CrI₃ Heterostructures. *npj 2D Mater. Appl.* **2019**, *3* (1), 3.
- (5) Soumyanarayanan, A.; Reyren, N.; Fert, A.; Panagopoulos, C. Emergent Phenomena Induced by Spin–Orbit Coupling at Surfaces and Interfaces. *Nature* **2016**, *539*, 509.
- (6) Mermin, N. D.; Wagner, H. Absence of Ferromagnetism or Antiferromagnetism in One- or Two-Dimensional Isotropic Heisenberg Models. *Phys. Rev. Lett.* **1966**, *17* (22), 1133–1136.
- (7) Huang, B.; Clark, G.; Navarro-Moratalla, E.; Klein, D. R.; Cheng, R.; Seyler, K. L.; Zhong, D.; Schmidgall, E.; McGuire, M. A.; Cobden, D. H.; et al. Layer-Dependent Ferromagnetism in a van Der Waals Crystal down to the Monolayer Limit. *Nature* **2017**, *546* (7657), 270–273.
- (8) Gong, C.; Li, L.; Li, Z.; Ji, H.; Stern, A.; Xia, Y.; Cao, T.; Bao, W.; Wang, C.; Wang, Y.; et al. Discovery of Intrinsic Ferromagnetism in Two-Dimensional van Der Waals Crystals. *Nature* **2017**, *546*, 265.
- (9) Wang, X.; Du, K.; Fredrik Liu, Y. Y.; Hu, P.; Zhang, J.; Zhang, Q.; Owen, M. H. S.; Lu, X.; Gan, C. K.; Sengupta, P.; et al. Raman Spectroscopy of Atomically Thin Two-Dimensional Magnetic Iron Phosphorus Trisulfide (FePS₃) Crystals. *2D Mater.* **2016**, *3* (3), 031009.
- (10) Tian, Y.; Gray, M. J.; Ji, H.; Cava, R. J.; Burch, K. S. Magneto-Elastic Coupling in a Potential Ferromagnetic 2D Atomic Crystal. *2D Mater.* **2016**, *3* (2), 025035.
- (11) Bonilla, M.; Kolekar, S.; Ma, Y.; Diaz, H. C.; Kalappattil, V.; Das, R.; Eggers, T.; Gutierrez, H. R.; Phan, M.-H.; Batzill, M. Strong Room-Temperature Ferromagnetism in VSe₂ Monolayers on van Der Waals Substrates. *Nat. Nanotechnol.* **2018**, *13* (4), 289–293.
- (12) Miao, N.; Xu, B.; Zhu, L.; Zhou, J.; Sun, Z. 2D Intrinsic Ferromagnets from van Der Waals Antiferromagnets. *J. Am. Chem. Soc.* **2018**, *140* (7), 2417–2420.
- (13) Chen, W.; Kawazoe, Y.; Shi, X.; Pan, H. Two-Dimensional Pentagonal CrX (X = S, Se or Te) Monolayers: Antiferromagnetic Semiconductors for Spintronics and Photocatalysts. *Phys. Chem. Chem. Phys.* **2018**, *20* (27), 18348–18354.
- (14) Hu, L.; Wu, X.; Yang, J. Mn₂C Monolayer: A 2D Antiferromagnetic Metal with High Néel Temperature and Large Spin–Orbit Coupling. *Nanoscale* **2016**, *8* (26), 12939–12945.
- (15) Mounet, N.; Gibertini, M.; Schwaller, P.; Campi, D.; Merky, A.; Marrazzo, A.; Sohler, T.; Castelli, I. E.; Cepellotti, A.; Pizzi, G.; et al. Two-Dimensional Materials from High-Throughput Computational Exfoliation of Experimentally Known Compounds. *Nat. Nanotechnol.* **2018**, *13* (3), 246–252.
- (16) Haastrup, S.; Strange, M.; Pandey, M.; Deilmann, T.; Schmidt, P. S.; Hinsche, N. F.; Gjerding, M. N.; Torelli, D.; Larsen, P. M.; Riis-Jensen, A. C.; et al. The Computational 2D Materials Database: High-Throughput Modeling and Discovery of Atomically Thin Crystals. *2D Mater.* **2018**, *5* (4), 042002.
- (17) Zhu, Y.; Kong, X.; Rhone, T. D.; Guo, H. Systematic Search for Two-Dimensional Ferromagnetic Materials. *Phys. Rev. Mater.* **2018**, *2* (8), 81001.

- (18) Jiang, S.; Shan, J.; Mak, K. F. Electric-Field Switching of Two-Dimensional van Der Waals Magnets. *Nat. Mater.* **2018**, *17* (5), 406–410.
- (19) Vatanserver, E.; Sarikurt, S.; Ersan, F.; Kadioglu, Y.; Üzengi Aktürk, O.; Yüksel, Y.; Ataca, C.; Aktürk, E.; Aktıncı, Ü. Strain Effects on Electronic and Magnetic Properties of the Monolayer α -RuCl₃: A First-Principles and Monte Carlo Study. *J. Appl. Phys.* **2019**, *125* (8), 083903.
- (20) Cao, T.; Li, Z.; Louie, S. G. Tunable Magnetism and Half-Metallicity in Hole-Doped Monolayer GaSe. *Phys. Rev. Lett.* **2015**, *114* (23), 236602.
- (21) Seixas, L.; Rodin, A. S.; Carvalho, A.; Castro Neto, A. H. Multiferroic Two-Dimensional Materials. *Phys. Rev. Lett.* **2016**, *116* (20), 206803.
- (22) Zhang, Z.; Wu, X.; Guo, W.; Zeng, X. C. Carrier-Tunable Magnetic Ordering in Vanadium–Naphthalene Sandwich Nanowires. *J. Am. Chem. Soc.* **2010**, *132* (30), 10215–10217.
- (23) Miao, N.; Xu, B.; Bristowe, N. C.; Zhou, J.; Sun, Z. Tunable Magnetism and Extraordinary Sunlight Absorbance in Indium Triphosphide Monolayer. *J. Am. Chem. Soc.* **2017**, *139* (32), 11125–11131.
- (24) Shi, L.; Zhao, T. Recent Advances in Inorganic 2D Materials and Their Applications in Lithium and Sodium Batteries. *J. Mater. Chem. A* **2017**, *5* (8), 3735–3758.
- (25) Kappera, R.; Voiry, D.; Yalcin, S. E.; Branch, B.; Gupta, G.; Mohite, A. D.; Chhowalla, M. Phase-Engineered Low-Resistance Contacts for Ultrathin MoS₂ Transistors. *Nat. Mater.* **2014**, *13* (12), 1128–1134.
- (26) Ogihara, N.; Ohba, N.; Kishida, Y. On/off Switchable Electronic Conduction in Intercalated Metal-Organic Frameworks. *Sci. Adv.* **2017**, *3* (8), No. e1603103.
- (27) Sood, A.; Xiong, F.; Chen, S.; Wang, H.; Selli, D.; Zhang, J.; McClellan, C. J.; Sun, J.; Donadio, D.; Cui, Y.; et al. An Electrochemical Thermal Transistor. *Nat. Commun.* **2018**, *9* (1), 4510.
- (28) Tang, J.; Bishop, D.; Kim, S.; Copel, M.; Gokmen, T.; Todorov, T.; Shin, S.; Lee, K.; Solomon, P.; Chan, K.; et al. ECRAM as Scalable Synaptic Cell for High-Speed, Low-Power Neuromorphic Computing. *2018 IEEE International Electron Devices Meeting (IEDM)*; IEEE, 2018; pp 13.1.1–13.1.4.
- (29) Coïc, L.; Spiesser, M.; Palvadeau, P.; Rouxel, J. Chromium (III) Oxyhalides: Magnetic and Optical Properties. Lithium Intercalation. *Mater. Res. Bull.* **1981**, *16* (2), 229–236.
- (30) Zhang, Q.; Luo, X.; Wang, L.; Zhang, L.; Khalid, B.; Gong, J.; Wu, H. Lithium-Ion Battery Cycling for Magnetism Control. *Nano Lett.* **2016**, *16* (1), 583–587.
- (31) Dasgupta, S.; Das, B.; Knapp, M.; Brand, R. A.; Ehrenberg, H.; Kruk, R.; Hahn, H. Intercalation-Driven Reversible Control of Magnetism in Bulk Ferromagnets. *Adv. Mater.* **2014**, *26* (27), 4639–4644.
- (32) Wei, G.; Wei, L.; Wang, D.; Chen, Y.; Tian, Y.; Yan, S.; Mei, L.; Jiao, J. Reversible Control of the Magnetization of Spinel Ferrites Based Electrodes by Lithium-Ion Migration. *Sci. Rep.* **2017**, *7* (1), 12554.
- (33) Mounet, N.; Gibertini, M.; Schwaller, P.; Campi, D.; Merkys, A.; Marrazzo, A.; Sohler, T.; Castelli, I. E.; Cepellotti, A.; Pizzi, G.; Marzari, N. Two-dimensional materials from high-throughput computational exfoliation of experimentally known compounds. *Materials Cloud Archive* **2018**, DOI: [10.24435/materials-cloud:2017.0008/v2](https://doi.org/10.24435/materials-cloud:2017.0008/v2).
- (34) Leong, C. C.; Pan, H.; Ho, S. K. Two-Dimensional Transition-Metal Oxide Monolayers as Cathode Materials for Li and Na Ion Batteries. *Phys. Chem. Chem. Phys.* **2016**, *18* (10), 7527–7534.
- (35) Meng, Y.; Liu, X.-W.; Huo, C.-F.; Guo, W.-P.; Cao, D.-B.; Peng, Q.; Dearden, A.; Gonze, X.; Yang, Y.; Wang, J.; et al. When Density Functional Approximations Meet Iron Oxides. *J. Chem. Theory Comput.* **2016**, *12* (10), 5132–5144.
- (36) Perdew, J. P.; Burke, K.; Ernzerhof, M. Generalized Gradient Approximation Made Simple. *Phys. Rev. Lett.* **1996**, *77* (18), 3865–3868.
- (37) Heyd, J.; Scuseria, G. E.; Ernzerhof, M. Hybrid Functionals Based on a Screened Coulomb Potential. *J. Chem. Phys.* **2003**, *118* (18), 8207–8215.
- (38) Toyoda, M.; Akai, H.; Sato, K.; Katayama-Yoshida, H. Curie Temperature of GaMnN and GaMnAs from LDA-SIC Electronic Structure Calculations. *Phys. Status Solidi C* **2006**, *3* (12), 4155–4159.
- (39) Webster, L.; Yan, J.-A. Strain-Tunable Magnetic Anisotropy in Monolayer CrCl₃, CrBr₃, and CrI₃. *Phys. Rev. B: Condens. Matter Mater. Phys.* **2018**, *98* (14), 144411.
- (40) Kumar, H.; Frey, N. C.; Dong, L.; Anasori, B.; Gogotsi, Y.; Shenoy, V. B. Tunable Magnetism and Transport Properties in Nitride MXenes. *ACS Nano* **2017**, *11* (8), 7648–7655.
- (41) Frey, N. C.; Kumar, H.; Anasori, B.; Gogotsi, Y.; Shenoy, V. B. Tuning Noncollinear Spin Structure and Anisotropy in Ferromagnetic Nitride MXenes. *ACS Nano* **2018**, *12* (6), 6319–6325.
- (42) Wang, D.; Liu, Y.; Meng, X.; Wei, Y.; Zhao, Y.; Pang, Q.; Chen, G. Two-Dimensional VS₂ Monolayers as Potential Anode Materials for Lithium-Ion Batteries and beyond: First-Principles Calculations. *J. Mater. Chem. A* **2017**, *5* (40), 21370–21377.
- (43) Pickard, C. J.; Needs, R. J. Ab Initio Random Structure Searching. *J. Phys.: Condens. Matter* **2011**, *23* (5), 053201.
- (44) Wang, Y.; Lv, J.; Zhu, L.; Ma, Y. Crystal Structure Prediction via Particle-Swarm Optimization. *Phys. Rev. B: Condens. Matter Mater. Phys.* **2010**, *82* (9), 94116.
- (45) Oganov, A. R.; Glass, C. W. Crystal Structure Prediction Using Ab Initio Evolutionary Techniques: Principles and Applications. *J. Chem. Phys.* **2006**, *124* (24), 244704.
- (46) Kabiraj, A.; Mahapatra, S. High-Throughput First-Principles-Calculations Based Estimation of Lithium Ion Storage in Monolayer Rhenium Disulfide. *Commun. Chem.* **2018**, *1* (1), 81.
- (47) Pickard, C. J.; Needs, R. J. Highly Compressed Ammonia Forms an Ionic Crystal. *Nat. Mater.* **2008**, *7*, 775.
- (48) Pickard, C. J.; Needs, R. J. Aluminium at Terapascal Pressures. *Nat. Mater.* **2010**, *9*, 624.
- (49) Putungan, D. B.; Lin, S.-H.; Kuo, J.-L. Metallic VS₂ Monolayer Polytypes as Potential Sodium-Ion Battery Anode via Ab Initio Random Structure Searching. *ACS Appl. Mater. Interfaces* **2016**, *8* (29), 18754–18762.
- (50) George, C.; Morris, A. J.; Modarres, M. H.; De Volder, M. Structural Evolution of Electrochemically Lithiated MoS₂ Nanosheets and the Role of Carbon Additive in Li-Ion Batteries. *Chem. Mater.* **2016**, *28* (20), 7304–7310.
- (51) Sato, K.; Bergqvist, L.; Kudrnovský, J.; Dederichs, P. H.; Eriksson, O.; Turek, I.; Sanyal, B.; Bouzerar, G.; Katayama-Yoshida, H.; Dinh, V. A.; et al. First-Principles Theory of Dilute Magnetic Semiconductors. *Rev. Mod. Phys.* **2010**, *82* (2), 1633–1690.
- (52) Henkelman, G.; Jónsson, H. Long Time Scale Kinetic Monte Carlo Simulations without Lattice Approximation and Predefined Event Table. *J. Chem. Phys.* **2001**, *115* (21), 9657–9666.
- (53) Xu, L.; Henkelman, G. Adaptive Kinetic Monte Carlo for First-Principles Accelerated Dynamics. *J. Chem. Phys.* **2008**, *129* (11), 114104.
- (54) Lee, G.-H.; Cui, X.; Kim, Y. D.; Arefe, G.; Zhang, X.; Lee, C.-H.; Ye, F.; Watanabe, K.; Taniguchi, T.; Kim, P.; et al. Highly Stable, Dual-Gated MoS₂ Transistors Encapsulated by Hexagonal Boron Nitride with Gate-Controllable Contact, Resistance, and Threshold Voltage. *ACS Nano* **2015**, *9* (7), 7019–7026.
- (55) Torelli, D.; Olsen, T. Calculating Critical Temperatures for Ferromagnetic Order in Two-Dimensional Materials. *2D Mater.* **2019**, *6* (1), 015028.
- (56) Song, C.; Xiao, W.; Li, L.; Lu, Y.; Jiang, P.; Li, C.; Chen, A.; Zhong, Z. Tunable Band Gap and Enhanced Ferromagnetism by Surface Adsorption in Monolayer Cr₂Ge₂Te₆. *Phys. Rev. B: Condens. Matter Mater. Phys.* **2019**, *99* (21), 214435.

- (57) Goodenough, J. B. An Interpretation of the Magnetic Properties of the Perovskite-Type Mixed Crystals $\text{La}_{1-x}\text{Sr}_x\text{CoO}_{3-d}$. *J. Phys. Chem. Solids* **1958**, *6* (2–3), 287–297.
- (58) Kanamori, J. Superexchange Interaction and Symmetry Properties of Electron Orbitals. *J. Phys. Chem. Solids* **1959**, *10* (2–3), 87–98.
- (59) Lan, M.; Xiang, G.; Nie, Y.; Yang, D.; Zhang, X. The Static and Dynamic Magnetic Properties of Monolayer Iron Dioxide and Iron Dichalcogenides. *RSC Adv.* **2016**, *6* (38), 31758–31761.
- (60) Kresse, G.; Hafner, J. Ab Initio Molecular Dynamics for Liquid Metals. *Phys. Rev. B: Condens. Matter Mater. Phys.* **1993**, *47* (1), 558–561.
- (61) Kresse, G.; Hafner, J. Ab Initio Molecular-Dynamics Simulation of the Liquid-Metal–Amorphous-Semiconductor Transition in Germanium. *Phys. Rev. B: Condens. Matter Mater. Phys.* **1994**, *49* (20), 14251–14269.
- (62) Kresse, G.; Furthmüller, J. Efficient Iterative Schemes for Ab Initio Total-Energy Calculations Using a Plane-Wave Basis Set. *Phys. Rev. B: Condens. Matter Mater. Phys.* **1996**, *54* (16), 11169–11186.
- (63) Kresse, G.; Furthmüller, J. Efficiency of Ab-Initio Total Energy Calculations for Metals and Semiconductors Using a Plane-Wave Basis Set. *Comput. Mater. Sci.* **1996**, *6* (1), 15–50.
- (64) Kresse, G.; Joubert, D. From Ultrasoft Pseudopotentials to the Projector Augmented-Wave Method. *Phys. Rev. B: Condens. Matter Mater. Phys.* **1999**, *59* (3), 1758–1775.
- (65) Krukau, A. V.; Vydrov, O. A.; Izmaylov, A. F.; Scuseria, G. E. Influence of the Exchange Screening Parameter on the Performance of Screened Hybrid Functionals. *J. Chem. Phys.* **2006**, *125* (22), 224106.
- (66) Dudarev, S. L.; Botton, G. A.; Savrasov, S. Y.; Humphreys, C. J.; Sutton, A. P. Electron-Energy-Loss Spectra and the Structural Stability of Nickel Oxide: An LSDA+U Study. *Phys. Rev. B: Condens. Matter Mater. Phys.* **1998**, *57* (3), 1505–1509.
- (67) Tkatchenko, A.; Scheffler, M. Accurate Molecular Van Der Waals Interactions from Ground-State Electron Density and Free-Atom Reference Data. *Phys. Rev. Lett.* **2009**, *102* (7), 73005.
- (68) Bultinck, P.; Van Alsenoy, C.; Ayers, P. W.; Carbó-Dorca, R. Critical Analysis and Extension of the Hirshfeld Atoms in Molecules. *J. Chem. Phys.* **2007**, *126* (14), 144111.
- (69) Marom, N.; Tkatchenko, A.; Rossi, M.; Gobre, V. V.; Hod, O.; Scheffler, M.; Kronik, L. Dispersion Interactions with Density-Functional Theory: Benchmarking Semiempirical and Interatomic Pairwise Corrected Density Functionals. *J. Chem. Theory Comput.* **2011**, *7* (12), 3944–3951.
- (70) Henkelman, G.; Arnaldsson, A.; Jónsson, H. A Fast and Robust Algorithm for Bader Decomposition of Charge Density. *Comput. Mater. Sci.* **2006**, *36* (3), 354–360.
- (71) Sanville, E.; Kenny, S. D.; Smith, R.; Henkelman, G. Improved Grid-Based Algorithm for Bader Charge Allocation. *J. Comput. Chem.* **2007**, *28* (5), 899–908.
- (72) Tang, W.; Sanville, E.; Henkelman, G. A Grid-Based Bader Analysis Algorithm without Lattice Bias. *J. Phys.: Condens. Matter* **2009**, *21* (8), 084204.
- (73) Yu, M.; Trinkle, D. R. Accurate and Efficient Algorithm for Bader Charge Integration. *J. Chem. Phys.* **2011**, *134* (6), 064111.
- (74) Momma, K.; Izumi, F. VESTA3 for Three-Dimensional Visualization of Crystal, Volumetric and Morphology Data. *J. Appl. Crystallogr.* **2011**, *44* (6), 1272–1276.
- (75) Cococcioni, M.; de Gironcoli, S. Linear Response Approach to the Calculation of the Effective Interaction Parameters in the LDA+U Method. *Phys. Rev. B: Condens. Matter Mater. Phys.* **2005**, *71* (3), 35105.
- (76) Nosé, S. A Unified Formulation of the Constant Temperature Molecular Dynamics Methods. *J. Chem. Phys.* **1984**, *81* (1), 511–519.
- (77) Hoover, W. G. Canonical Dynamics: Equilibrium Phase-Space Distributions. *Phys. Rev. A: At., Mol., Opt. Phys.* **1985**, *31* (3), 1695–1697.
- (78) Grimme, S.; Antony, J.; Ehrlich, S.; Krieg, H. A Consistent and Accurate Ab Initio Parametrization of Density Functional Dispersion Correction (DFT-D) for the 94 Elements H–Pu. *J. Chem. Phys.* **2010**, *132* (15), 154104.